Robust Path-Following Control for High Altitude Long Endurance Aircraft

Christian Weiser *
Institute of System Dynamics and Control,
German Aerospace Center (DLR), 82234 Weßling, Germany

Daniel Ossmann †
Department of Mechanical, Automotive and Aeronautical Engineering,
Munich University of Applied Sciences HM, 80335 Munich, Germany

Harald Pfifer ‡
Chair of Flight Mechanics and Control,
TU Dresden, 01069 Dresden, Germany

I. Introduction

High Altitude Long Endurance (HALE) aircraft are usually operated on multi-day missions, where the goal is to track a specific reference flight path whilst flying at the airspeed for maximum aerodynamic efficiency. The described HALE aircraft type is propelled by electric motors and propellers driven by a solar generator and batteries. In order to achieve a positive energy balance over a 24 hour cycle, the structural weight is minimized, which results in a very narrow airspeed envelope. This is extremely critical, as it requires accurate tracking of the airspeed reference throughout maneuvering and especially during disturbances, e.g. gusts or continuous turbulence.

The contribution of this article is the proposal of an observer-based mixed sensitivity flight path-tracker and its simulation-based verification. The observer-based design has the advantage that including anti-windup becomes a fairly straightforward task. The design follows an approach presented in [1, 2]. The resulting flight path-tracker is connected to an inner cascade consisting of an attitude controller introduced in [3]. With this control system setup, non-linear simulations and Monte Carlo (MC) analysis are performed for verification.

The first part of the article introduces the considered HALE aircraft model, which is currently being developed by the German Aerospace Center [4–6]. The presented configuration is currently being built and will be flight-tested within the next years. In Sec. III the observer-based mixed sensitivity control design method [7] is introduced. Furthermore, anti-windup methods are discussed, which are crucial for a successful implementation in the aircraft path-tracking application, as saturations especially in the thrust command channel are expected. In Sec. IV, the presented flight path-tracker mixed-sensitivity synthesis is applied to the longitudinal aircraft dynamics model, which is already augmented by a previously designed pitch attitude tracker. The mentioned anti-windup compensation is added to obtain

*Research Assistant, christian.weiser@dlr.de, AIAA Member
†Professor, daniel.ossmann@hm.edu, AIAA Senior Member
‡Professor, harald.pfifer@tu-dresden.de

Fig. 1 Artistic HALE aircraft representation. Copyright: German Aerospace Center (DLR), 2023.

a control design, which shows adequate performance even in presence of thrust saturation. Following, the obtained mixed-sensitivity flight path-tracker is verified in the non-linear domain for a realistic ascent scenario. The climb from ground to the operating altitude including wind disturbance in the form of Continuous Turbulence (CT) is analyzed. A MC simulation is performed, where besides the robustness to external disturbance, the robustness of the controller against model uncertainties is proven. Finally, in Sec. VI the obtained results are compared to the results obtained with a previously implemented Total Energy Control System (TECS) algorithm designed in [3].

II. HALE Aircraft model

Fig. 1 illustrates an example design of the described HALE aircraft [4]. The solar powered aircraft is designed for a cruise altitude of 18 km with a service ceiling of 20 km. Mission scenarios for HALE aircraft are similar to satellites, e.g. earth observation or communication, and require the platform to stay airborne in the stratosphere from multiple days up to several weeks. Due to its very light-weight construction, the aircraft has a speed envelope of approximately 6.5 m/s up to 15.5 m/s in equivalent airspeed difference from stall to maximum airspeed. The nominal operating speed is the velocity for best endurance, which is defined by the aerodynamic properties and has a value of approx. 9 m/s. The mathematical model of the HALE aircraft includes non-linear rigid body aircraft equations of motion

$$\begin{bmatrix} M_b(\dot{V}_b + \Omega_b \times V_b) \\ I_b(\dot{\Omega}_b + \Omega_b \times (I_b \Omega_b) \end{bmatrix} = \Phi_{ba} P_a^{\text{ext}}, \tag{1}$$

with the aircraft's mass M_b, its moment of inertia I_b, and the linear and rotational velocities V_b, Ω_b. External forces and moments P_a^{ext} on the right hand side are calculated as described in [8]. The model is augmented with a second order linear structural model

$$M_{ff}\ddot{u}_f + D_{ff}\dot{u}_f + K_{ff}u_f = \Phi_{fa} P_a^{\text{ext}}, \tag{2}$$

provided by [9] and [10]. The structural dynamics in (2) are a second order differential equation with masses M_{ff},

stiffness matrix K_{ff}, damping matrix D_{ff} and the modal displacement u_f. The matrix Φ_{ba} describes the transfer from aerodynamic into the body-fixed coordinate frame, Φ_{fa} into the modal coordinates. The aerodynamic forces and moments are modeled via the vortex lattice method (VLM). A detailed description on these aerodynamics can be found in [8].

Following the non-linear model generation, a linear model of the aircraft in the standard form

$$\left[\begin{array}{c} \dot{x} \\ \hline y \end{array}\right] = \left[\begin{array}{c|cc} A & B_u & B_d \\ \hline C & D_u & D_d \end{array}\right] \left[\begin{array}{c} x \\ \hline u \\ \\ d \end{array}\right] \tag{3}$$

with the state vector x, its derivative $\dot{x}$, the input vector u, the output vector y, the disturbance d and the state space matrices A, B_u, B_d, C, D_u, and D_d, enables the application of a linear control design method. Therefore, the non-linear aircraft equations are linearized at steady state operating points consisting of the minimal operating airspeed for best aerodynamic efficiency V_{eas} = 9m/s and altitude h = 18 km, which corresponds to approximately Flight Level (FL) 600 (altitude in 100 ft). A low order approximation of the aircraft's longitudinal dynamics is obtained via truncation of the lateral modes as well as flexible modes far beyond the actuator bandwidth. In the derived aircraft model for the controller design, the state vector x includes the angle of attack α, pitch rate q, pitch attitude θ, airspeed V, the involved structural modes U_f and their derivatives dU_f. The input vector u includes the elevator deflection η and thrust setting T and the output vector y includes pitch angle θ, Flight Path Angle (FPA) γ, and the true airspeed V_{TAS}. Finally, the disturbance d is a wind disturbance on the aircraft. The eigenvalues of the linear aircraft model are depicted in Fig. 2 from ground to maximum operating altitude at the design airspeed. Fig. 2a shows the first wing bending, phugoid and short period modes, where the wing bending mode is a complex pole pair with increasing frequency, starting at 4 rad/s. Simultaneously, the damping decreases slightly. Between FL400 and FL600 (12 - 18 km), the short period becomes an oscillatory mode at around 8 rad/s and the branches of the wing bending and short period modes overlap. For the phugoid motion, which is depicted again in the zoom in Fig. 2, the frequency decreases slightly whereas the damping coefficient becomes almost zero for high altitudes. Especially the phugoid mode shows a rapidly decreasing damping coefficient for increasing altitude, thus the linear model at maximum altitude (FL600) is chosen for the robust controller design in the expectation that this will lead to the best (and most robust controller) for the full flight envelope.

Note the linear model contains a total number of 8 flexible aircraft modes, which are not visible in Fig. 2 due to their high frequencies.

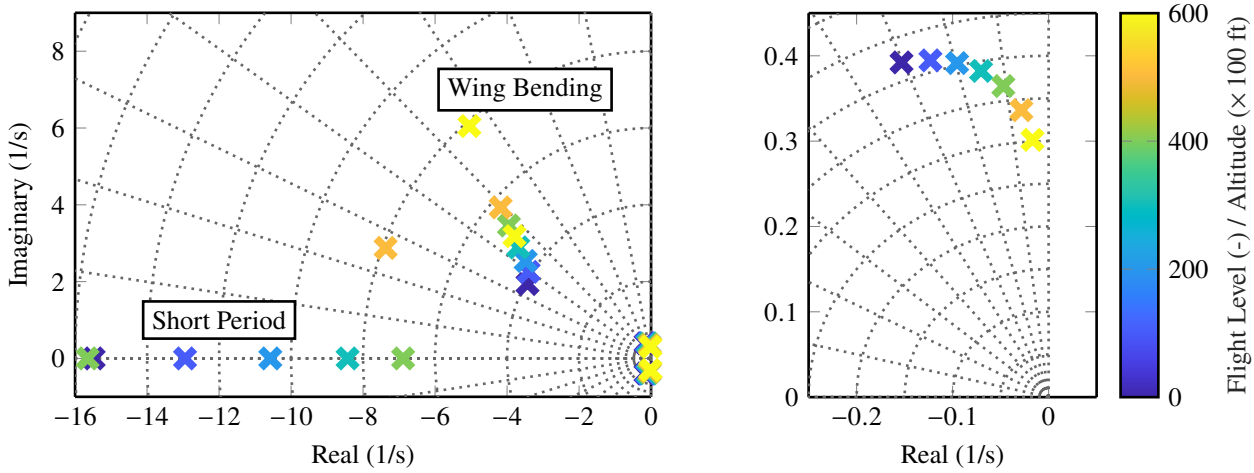

(a) Pole-zero map of the short period, first symmetric wing bending and phugoid modes.

(b) Zoom onto the phugoid mode.

Fig. 2 Pole-zero map of the longitudinal aircraft dynamics over altitude at design airspeed (V_{eas} = 9 m/s).

III. Observer Based Mixed Sensitivity Control with Anti-Windup

Shaping closed loop sensitivity functions through minimization of the H_∞-norm is a common approach for control design in literature, see e.g. [11]. A common interconnection for designing the controller $K(s)$ is given in terms of a mixed sensitivity problem in Fig. 3. The considered plant $G(s)$ can be augmented by an explicit disturbance model $G_d(s)$, as depicted in the figure. The mixed sensitivity formulation is the weighted closed loop system's H_∞-norm of the feedback interconnection in Fig. 3, which can be noted as follows:

$$\begin{bmatrix} z_e \\ z_u \end{bmatrix} = \begin{bmatrix} W_e V_e^{-1} & 0 \\ 0 & W_u V_u^{-1} \end{bmatrix} \begin{bmatrix} S & -SG_d \\ KS & -KSG_d \end{bmatrix} \begin{bmatrix} V_e & 0 \\ 0 & W_d \end{bmatrix} \begin{bmatrix} r \\ d \end{bmatrix}, \tag{4}$$

where $S = (I + GK)^{-1}$ denotes the output sensitivity function. The weighting scheme differentiates between frequency dependent weights denoted by W and constant scaling factors denoted by V. It is taken from [12]. The weight function W_e enforces the frequency requirements on the sensitivity function, i.e. tracking and disturbance rejection at low frequencies. The weight W_u shapes the control input u through KS. It can be used to enforce an appropriate roll-off of the controller K. The scalings V_e, V_u and V_d can be used for setting the maximum allowable control error, control effort and disturbance, respectively.

A. Observer-based mixed sensitivity synthesis

In general, solving the output feedback mixed sensitivity problem defined in the previous section results in a full order controller without specific structure. However, the output feedback problem can be separated in an observer and a state-feedback problem while retaining the closed loop shaping characteristics. The main result of this separation goes

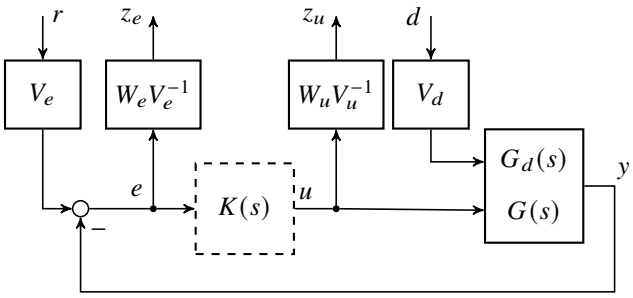

Fig. 3 Generic H_∞ weighting structure.

back to H_∞ loop-shaping by Glover and McFarlane [13] and [14]. More recently, observer-based mixed sensitivity control techniques have been proposed for linear parameter varying systems [7] and linear time varying systems [15]. The structure of the controllers has the form

$$\left[\begin{array}{c} \dot{\xi} \\ \hline u \end{array}\right] = \left[\begin{array}{c|c} A + BF + LC & L \\ \hline F & 0 \end{array}\right] \left[\begin{array}{c} \xi \\ \hline e \end{array}\right]. \tag{5}$$

The synthesis approach is based on sequentially solving a normalized coprime factorization and a state feedback problem as formalized in the following theorem.

Theorem 1 (observer-based controller synthesis)**.** *Let G be a linear time invariant (LTI) system. There exists an observer-based controller K as in (5) such that $||\mathcal{F}(G,K)|| \leq \gamma$ if there exist symmetric matrices $Z \in \mathbb{R}^{n_x \times n_x}$ and $Y \in \mathbb{R}^{n_x \times n_x}$ such that*

$$Z > 0 \tag{6a}$$

$$\begin{bmatrix} ZA + A^TZ - C^TC & ZB_d \\ B_d^TZ & -I \end{bmatrix} < 0 \tag{6b}$$

and

$$\gamma > 1 \tag{7a}$$

$$Y > 0 \tag{7b}$$

$$\begin{bmatrix} YA^T + AY - \gamma B_u B_u^T & -YC^T & -Z^{-1}C^T \\ -CY & -\gamma I & I \\ -CZ^{-1} & I & -\gamma I \end{bmatrix} < 0. \tag{7c}$$

Proof. Equations (6) are the existence conditions for the normalized left coprime factorization $M^{-1}N_d = G_d$ [14].

They yield the observer gain $L = -Z^{-1}C^T$ and establish

$$\hat{e} = Mr - N_d d. \tag{8}$$

Equations (7) are the state feedback existence conditions of Theorem 3 in [7] for the generalized plant formulated as

$$\left[\begin{array}{c} \dot{\xi} \\ \hline e \\ u \\ \xi \end{array}\right] = \left[\begin{array}{c|cc} A & L & B \\ \hline -C & I & 0 \\ 0 & 0 & I \\ I & 0 & 0 \end{array}\right] \left[\begin{array}{c} \xi \\ \hline \hat{e} \\ u \end{array}\right]. \tag{9}$$

They yield $F = -\gamma B_u^T Y^{-1}$ and establish

$$\left[\begin{array}{c} e \\ u \end{array}\right] = \left[\begin{array}{c} (I + GK)^{-1} \\ K(I + GK)^{-1} \end{array}\right] M^{-1}\hat{e}. \tag{10}$$

It was previously shown in [7] that the combination of (8) and (10) recovers the original mixed sensitivity problem (4). The property $\|[M \quad N_d]\| = 1$ of the normalized coprime factorization implies $\|[-N_d \quad M]\| = 1$ and it follows from submultiplicativity of the induced $\mathcal{L}_2$-norm that

$$\begin{aligned} \left\| \left[\begin{array}{cc} -SG_d & S \\ -KSG_d & KS \end{array}\right] \right\| &= \left\| \left[\begin{array}{c} S \\ KS \end{array}\right] M^{-1} \left[\begin{array}{cc} -N_d & M \end{array}\right] \right\| \\ &\leq \left\| \left[\begin{array}{c} S \\ KS \end{array}\right] M^{-1} \right\| \left\| [-N_d \quad M] \right\| \\ &= \left\| \left[\begin{array}{c} S \\ KS \end{array}\right] M^{-1} \right\|. \end{aligned} \tag{11}$$

□

Theorem 1 can be used to obtain a controller K as in (5) that minimizes the weighted mixed sensitivity problem depicted in Fig. 3. A step by step guide on the solution of the weighted problem is detailed in [7]. The key point is that the resulting controller has now a specific structure as shown in Fig. 4, where all the dynamics are in the observer O. Additionally, the observer itself is also highly structured as shown in Fig. 5. The observer consists of an integral

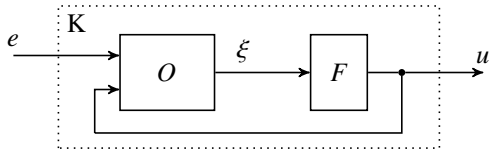

Fig. 4 Observer-based controller.

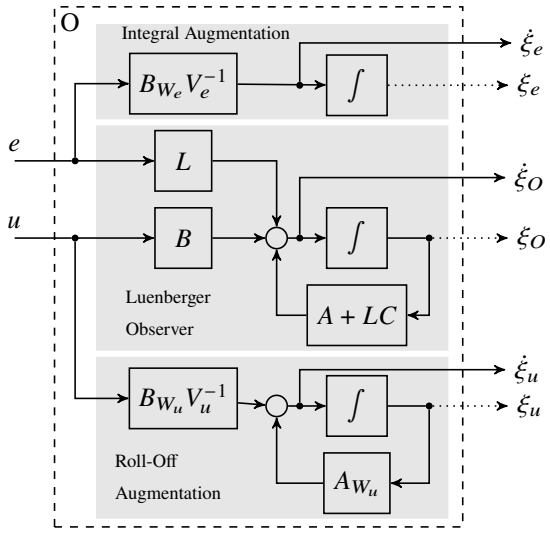

Fig. 5 Weight-augmented observer with state derivative output.

augmentation through the weighting W_e, a roll-off augmentation through W_u and a classical Luenberger observer. This structure is specifically advantageous for adding anti-windup schemes as the integrators appear explicitly in the structure.

B. Anti-windup strategy

In a first step, the obtained observer-based controller is slightly modified in order to isolate the integrator. To achieve this, instead of the observer states ξ, the state derivatives $\dot{\xi}$ can be removed from the structured observer, as seen in Fig. 5. Then, the multiplication with the observer gain

$$\dot{u} = F\dot{\xi} \tag{12}$$

is done as in the initial observer structure in Fig. 4. The integrator is then placed behind the feedback gain F in Fig. 6. Now that the integrator has been separated from the multi-input-multi-output (MIMO) controller's feedback gains, the implementation of an anti-windup method is a straight-forward task. As the integrator states in Fig. 6 have now the physical meaning of the controller output, e.g. the anti-windup methods clamping or back-calculation can be used [16]. Clamping simply limits the integrator output to certain minimum or maximum values and stops the integration as long as the integrator output is in limit. The back-calculation method [16] is convenient to use for preventing windup of the integrator in case of a variable or externally defined limit.

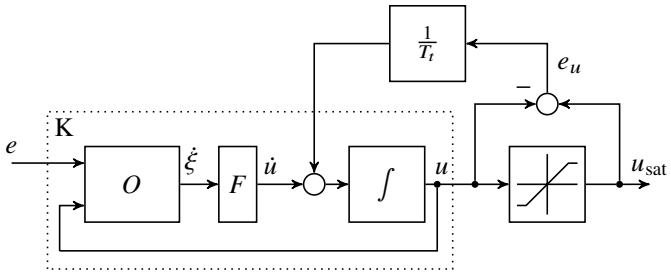

Fig. 6 Back-calculation anti-windup scheme for usage with an observer-based controller.

Fig. 6 shows the principle of the back-calculation method, where the difference of the unlimited and limited actuation commands, $e_u = u - u_{\text{sat}}$ is inserted into the integrator input. This gives the equation for the integrator input i:

$$i = \dot{u}\frac{1}{T_i} + e_u\frac{1}{T_t}, \tag{13}$$

where T_i is the integrator time constant, T_t is the time constant of the back-calculation block. In steady state, also during saturation, the feedback of e_u keeps the integrator input at zero, thus (13) can be reformulated to

$$e_u = -\dot{u}\frac{T_t}{T_i}. \tag{14}$$

Together with $e_u = u_{\text{sat}} - u$ this gives

$$u = u_{\text{sat}} + \dot{u}\frac{T_t}{T_i}. \tag{15}$$

Thus, during saturation the integrator output equals the limit value plus the derivative of the control variable u, which is calculated via the observer and the static gain F.

IV. Observer-Based Path-Tracker Design with Anti-Windup for a HALE Aircraft

In this section the methodology for the observer based mixed sensitivity control design presented in section III is applied to a linear model of DLR's HALE aircraft [4].

A. Controller design

For the MIMO controller synthesis, the linear model of the operating point at maximum speed and maximum altitude is chosen since this point shows the highest frequency and lowest damping values of the pitch motion throughout the flight envelope. It is assumed that deriving a controller ensuring adequate closed loop stability and performance for this "worst-case" point, the controller also performs well for the lower flight speeds and lower altitudes. The block diagram in Fig. 7 illustrates the interconnection of the flight path-tracker with an inner-loop feedback controller and the the longitudinal aircraft dynamics G_{lon}. The reference variables for the flight path-tracker are the FPA γ and the

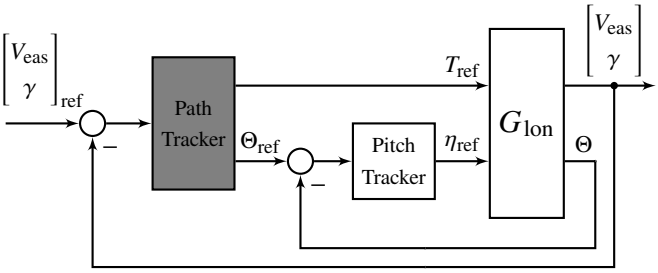

Fig. 7 Controller structure illustration.

equivalent airspeed V_{eas}. The flight path-tracker outputs are the reference pitch attitude Θ_{ref}, which is fed to the inner loop controller, and the reference thrust, which is calculated as thrust to weight ratio inside the controller.

First, the pitch-tracker of standard proportional-integral form

$$\eta_{\text{ref}} = k_p e_\Theta + k_i \int e_\Theta \text{dt} \tag{16}$$

with the two controller gains k_p and k_i is designed as an inner loop controller. For this inner loop the reference variable is the pitch attitude Θ_{ref}, which is commanded by the flight path-tracker. The control error is obtained as $e_\Theta = \Theta_{\text{ref}} - \Theta$, with the feedback of the pitch angle Θ. The pitch tracker is designed with a bandwidth of 2 rad/s in order to ensure a fast and well damped inner system. More details on the actual inner loop controller design and its specifications are provided in [3].

For the flight path-tracker controller synthesis, the weighting scheme depicted in Fig. 3 is used. The required scaling of the inner loop dynamics for the H_∞ controller design is considered via $V_e = [1, 5\pi/180]I_2$ on the inner loop outputs, i.e., assuming a maximum velocity deviation of 1 m/s from the trim point and a maximum FPA deviation of 5 degrees. $V_d = 1$ m/s is equally applied for the disturbance input. For the input scaling of the inner loop system $V_u = [0.2, 5\pi/180]I_2$ is applied, i.e., a maximum authority of 0.2 as achievable thrust to weight ratio and a maximum of 5 degrees in pitch attitude reference.

For the performance weight W_e a bandwidth of 0.25 rad/s is targeted in both the velocity and the FPA channel. These 0.25 rad/s are well below the the pitch tracker's inner loop bandwidth of of 2 rad/s as well as the available bandwidth of the propulsion system, which is assumed to be above 1 rad/s. To support this, the roll-off filter W_u is selected with a bandwidth of 0.5 rad/s in both input channels. The resulting closed loop sensitivity and complementary sensitivity functions for the velocity and for the FPA channel are depicted in Fig. 8. From the figure the values for the controller bandwidth can be read to 0.4 rad/s in the velocity channel and 0.2 rad/s in the FPA channel. For the anti-windup augmentation, the parameter T_t in (13)-(15) is selected equal to the integrator time constant $T_i = 1$.

The achieved MIMO controller design is assessed in the linear domain for robustness in terms of one loop at a time gain and phase margins as well as disk margins as defined in [17, 18]. The controller was designed with a single LTI

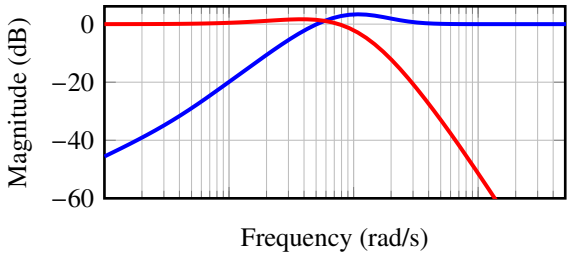

(a) Equivalent airspeed channel.

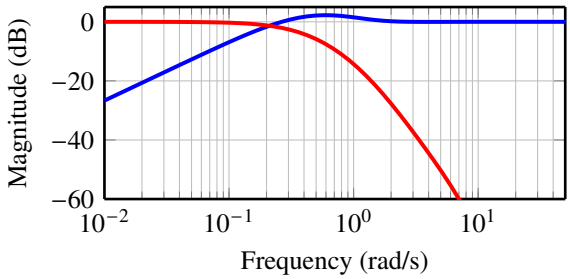

(b) Flight path angle channel.

Fig. 8 Output sensitivity S (——) and complimentary sensitivity T (——) for the mixed-sensitivity flight path-tracker.

model at the operating conditions of 18 km altitude (FL600) and nominal operating airspeed. In Fig. 9 the disk margin for the loop transfer function $L = PK$ is depicted with the obtained controller K for the plant over altitude from 0 to 18 km. It is shown, that even for the ground condition, which deviates most from the design point, a disk gain margin > 6 dB and a disk phase margin of 45 deg are obtained, which is sufficient.

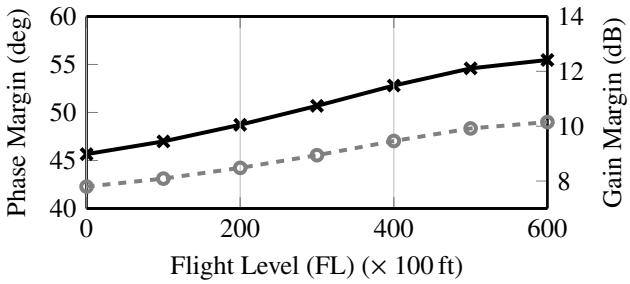

Fig. 9 Minimum disk gain (- ⊙ -) and phase (—×—) margins of the loop transfer functions over altitude with single point design observer-based controller.

B. Non-linear simulation

The verification of the designed control system is performed using a non-linear model of the aircraft dynamics as presented in (1) and (2) augmented with the controller designed herein. The results of the non-linear closed loop simulations are presented in Fig. 10. The simulated scenario is a climb maneuver between $t = 10$ s until $t = 35$ s with a step command of 5 deg in FPA at 10 s and a second step, which returns the FPA command to zero at 35 s. The velocity

command remains at the best endurance airspeed for the whole maneuver. Fig. 10 compares the described maneuver for three simulation scenarios: nominal, where no thrust saturation occurs, (blue), with an artificially lowered thrust saturation of 150 N per engine with anti-windup on (green) and without anti-windup (red). Note that this artificial limit is chosen to allow for a better comparison of the result. The actual saturation limit of the engine is higher than the presented one. The nominal case (blue) shows adequate performance with a settling time of less than 20 s and no overshoot of the FPA response in the first diagram. This corresponds to the design goal defined in the mixed-sensitivity controller design. Furthermore, the cross-coupling between flight path command and airspeed, visible via the second diagram, is limited to 0.3 m/s. Considering linearity, this corresponds to about 0.06 m/s per degree of FPA command. The achieved (blue) and required thrust (black) are depicted in the third diagram. In the scenario without saturation the lines are nearly exactly above each other, as only the linear engine dynamics lie between the two signals.

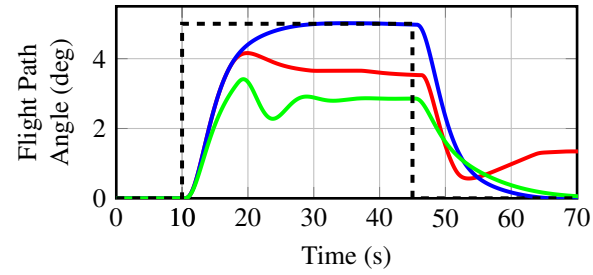

(a)

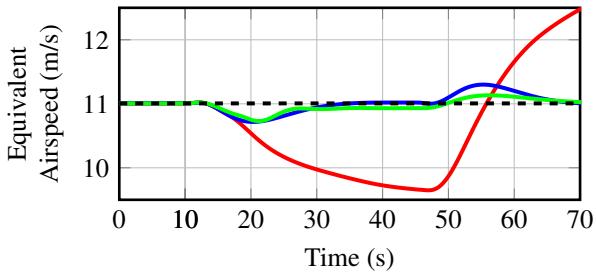

(b)

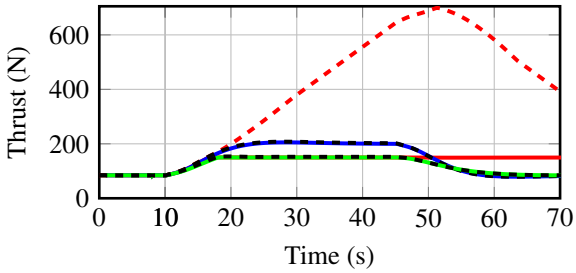

(c)

Fig. 10 Non-linear closed loop simulation of the observer-based flight path-tracker during nominal operation (——) and with thrust control in saturation without anti-windup (——) and with anti-windup (——).

As mentioned above, in a second scenario the thrust is limited to a maximum value of 150 N. The saturation is

clearly visible in the third diagram, as for both, the scenario with and without anti windup the actual trust signals do not increase over 150 N (green and solid red lines). In the scenario without anti-windup, however, severe integrator windup is encountered in the thrust command (red dashed line in third diagram). This windup effect results in large airspeed (red line in second diagram) deviations and no adequate tracking even after the flight path command is taken back to zero at 35 s in the simulation. To avoid this undesired behavior, anti-windup augmentation in the form of back-calculation is introduced and added to the observer-based controller. The green lines in Fig. 10 depict this scenario, which shows similar small deviation of the airspeed from the command value during the FPA command input as seen in the nominal case (green vs. blue lines in the middle plot in Fig. 10). Moreover, as soon as the flight path reference returns to zero, the nominal controller performance is restored instantaneously. The FPA is tracked with a higher control error during the FPA command when anti-windup is active. This is due to the smaller velocity error. In case no anti-windup is used the increased velocity error induces a higher pitch angle reference θ_{ref} due to the cross-coupling in the controller.

V. Non-linear Verification

To verify that the designed flight path-tracker is capable of safely controlling the HALE during an ascent from sea level to its operating altitude of 18 km, a realistic ascent scenario has been created. The simulation scenario starts the aircraft's climb at sea level and continues up to its operating altitude at Flight Level (FL) 600. As especially the climb phase is considered the most critical part of the mission, it is particularly interesting for the verification of the flight path-tracker. In a second step, a MC simulation is conducted, which investigates the closed loop reaction w.r.t. parametric uncertainties and disturbances. For both verification scenarios, the ascent and the MC simulation, CT is assumed as disturbance signal. The CT model is implemented according to the specifications for flying qualities of manned aircraft [19]. The turbulence intensity vs. altitude is depicted in Fig. 11. The HALE aircraft's airspeed range in equivalent airspeed is one magnitude below the values for common transport aircraft. This means, that especially at sea level, where true airspeed equals equivalent airspeed and the highest turbulence intensities occur, it is very unlikely that the HALE is capable of coping "medium" or "high" intensities from [19]. Thus, for the verification activities "light" turbulence in Fig. 11 is assumed as input disturbance. For the implementation of the CT for the VLM aerodynamic model used in the simulations the implementation described in [20, 21] is used.

A. Simulation of a realistic Ascent Scenario

For the first verification activity, the simulation described in Sec. IV.B is extended with an input for CT in the vertical and lateral true airspeed components and the command input is a climb at a constant FPA γ of 5 deg. This is just above the maximum performance that the aircraft can achieve. Since the commanded FPA is slightly larger than the maximum aircraft performance, the thrust is in saturation at all times. This poses another difficulty as the path-tracking controller is left with only the pitch attitude as unsaturated control variable. The climb power is limited by the maximum

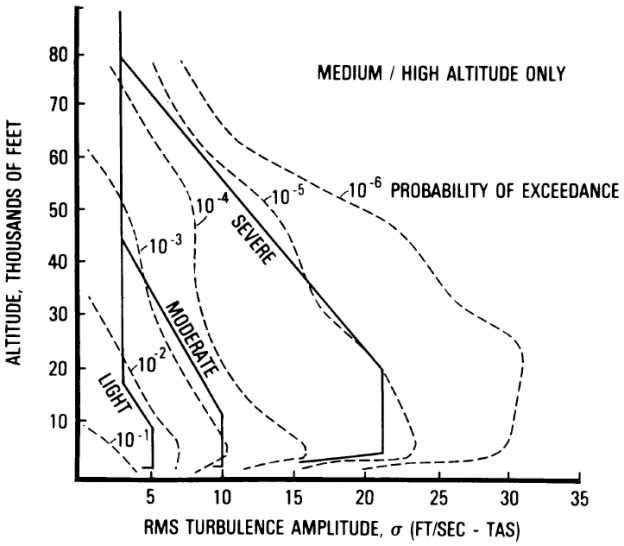

Fig. 11 Turbulence intensity vs. altitude. Reprinted from MIL-STD-1797A, Appendix A (public release, unlimited distribution) [19].

engine current at low altitudes and the maximum power and engine rotational speed at high altitudes.

The results of the ascent simulation are depicted in Fig. 12. It can be seen that the aircraft requires a time of approx. 5 h to reach its operating altitude. The left upper plot shows the equivalent airspeed and the envelope limits, which are maintained although it can be seen that the safety margin towards the never-exceed velocity V_{NE} is narrow at about $t = 20'$. The true airspeed plot below shows the increase in V_{tas}, which is together with the decreasing turbulence amplitude the main reason for the decreasing effect of the disturbance onto the system performance towards higher altitudes in the simulation. This can also be monitored in the right upper plot, where the FPA deviation is large (up to 20 deg), which poses a second difficulty for the path-tracking controller, as the disturbance leads to abrupt and large deviations from the set point. It can be concluded, that on the one hand especially the first 10 km of the climb segment are critical for the aircraft, as equivalent airspeed deviation is close to the boundaries. On the other hand, for altitudes above 10 km the visible disturbance in the aircraft reaction almost vanishes and the disturbance becomes uncritical for keeping the aircraft within the flight envelope.

B. Monte-Carlo based verification of the observer-based flight path-tracker

For further verification of the robust observer-based flight path-tracker with respect to parametric uncertainties and disturbance, a MC simulation is performed. For the MC simulation, the same climb scenario with thrust saturation as presented in Sec. V.A is used. For the MC simulation, basic longitudinal stability derivatives as well as mass and center of gravity (c.g.) uncertainties are added to the model. An overview of the used uncertain parameters in the MC simulation and their standard derivatives, respectively minimum and maximum values are listed in Tab. 1 where $C_{m\alpha}$ is the pitch moment due to an angle of attack change, C_{mq} the pitch moment due to a pitch rate and $C_{m\eta}$ the pitch moment

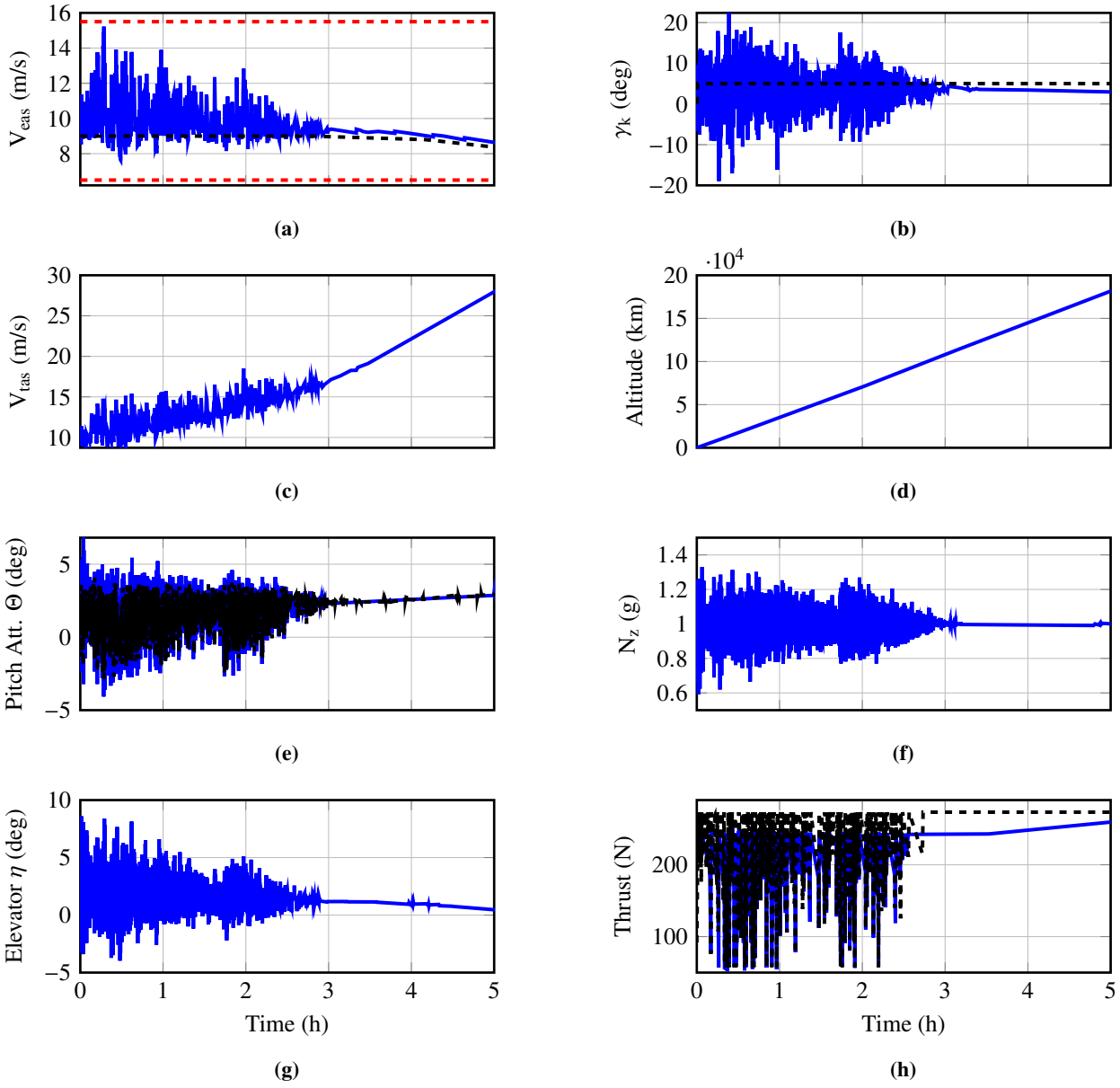

Fig. 12 Non-linear simulation of HALE aircraft ascent (——) from ground to 18 km (FL600), references (- - -) to the TECS controller and to the inner loop and thrust command.

resulting from an elevator deflection. The equivalent airspeed command is, as presented in Sec. V.A, kept constant at $V_{eas,\,com} = 9$ m/s, which is the speed for best endurance. The altitude is varied from 0 to 18 km. With a total number of $n = 20000$ simulations, the results in Fig. 13 are generated. The figure shows the probability distribution function (PDF) and cumulative distribution function (CDF) for minimum and maximum equivalent airspeed during each simulation. The red areas in the CDF plots show the stall respectively never exceed airspeed and a probability of exceedance greater than 1e-3. It can be seen, that a probability of exceedance of less than 1e-3 for stall and never exceed airspeed can be achieved with the model and the assumed uncertainties.

Table 1 Input parameter distributions for the Monte-Carlo analysis.

Parameter	Distribution	Min	Max	σ
Flight Level (x100 ft)	Uniform (discrete)	0	600	
Mass Uncertainty (%)	Normal	-3	+3	1
CG Variation in x-direction (m)	Normal	-0.3	+0.3	0.05
Δ $C_{m\alpha}$ (%)	Normal	-15	+15	10
Δ C_{mq} (%)	Normal	-15	+15	10
Δ $C_{m\eta}$ (%)	Normal	-15	+15	10

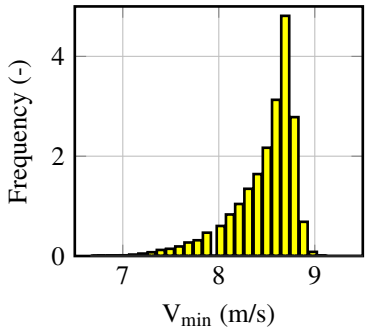

(a) PDF of the minimum equivalent airspeed.

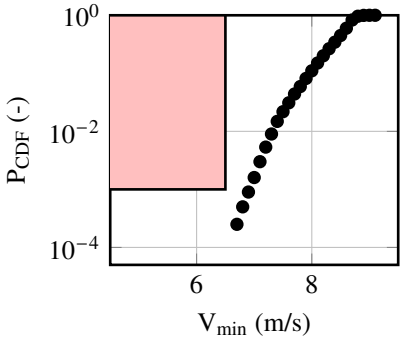

(b) CDF of the minimum equivalent airspeed.

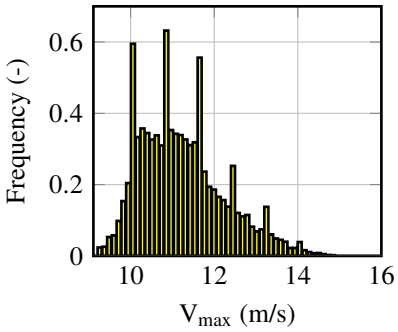

(c) PDF of the maximum equivalent airspeed.

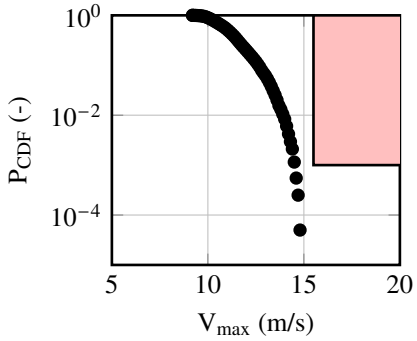

(d) CDF of the maximum equivalent airspeed.

Fig. 13 Monte-Carlo simulation results for the robust flight path-tracker.

VI. Comparison to Total Energy Control

A longitudinal autopilot concept, which offers decoupling of airspeed and FPA is the Total Energy Control System TECS. The control strategy was initially introduced in the early 80's by A. Lambregts [22] and subsequently flight tested by NASA and Boeing [23]. It has been applied in previous HALE design projects as well as proven in flight tests [24]. In this section, the TECS design is presented briefly and compared to the robust flight path-tracker approach.

The TECS control law is based on the principal of the overall energy of the aircraft, i.e. $E = E_{\text{pot}} + E_{\text{kin}}$. With the small angle approximation $\dot{h} \simeq V\gamma$ the derivative of the total energy equation is given by

$$\dot{E} = mg\dot{h} + mV\dot{V} \simeq mgV\left(\gamma + \frac{\dot{V}}{g}\right). \tag{17}$$

Assuming that the increase in drag ΔD is small compared to the thrust increase ΔT in (18), an energy change $\dot{E}$ can directly be related to a thrust command T_{cmd}. Introducing the specific total energy rate $\dot{E_S} = \dot{E}/(mgV)$ and considering the control errors in FPA and equivalent airspeed result in

$$\begin{aligned} \Delta\dot{E_S} &= (\gamma_{\text{cmd}} - \gamma) + (\dot{V}_{\text{cmd}} - \dot{V})/g \\ &= (\Delta T_{\text{cmd}} - \Delta D)/(mg) \simeq T_{\text{cmd}}/(mg), \end{aligned} \tag{18}$$

describing the commanded specific energy rate change. Finally, a proportional-integral (PI) control law for the thrust can be defined by

$$\frac{T_{\text{cmd}}}{mg} = K_{TI} \int \Delta\dot{E_S} dt - K_{TP}\dot{E_S}. \tag{19}$$

To derive the second command signal $\delta\Theta_{\text{cmd}}$, the specific energy distribution $\dot{D}_s$ between kinematic and potential energy rate is simply defined by the difference of the two energy types,

$$\dot{D_S} = -E_{\text{S,pot}} + E_{\text{S,kin}} = -\gamma + \frac{\dot{V}}{g}. \tag{20}$$

The specific energy distribution can be fed back due to the substitution in (20) by the measurements γ and $\dot{V}$. To enable a feedback loop the measurements are subtracted from their demands

$$\Delta\dot{D_S} = \dot{D}_{S,\text{cmd}} - \dot{D_S} = -(\gamma_{\text{cmd}} - \gamma) + \frac{(\dot{V}_{\text{cmd}} - \dot{V})}{g}. \tag{21}$$

Finally, using the assumption that commanded energy distribution rate is proportional to the commanded pitch attitude [22], i.e., $\Delta\dot{D_S} \propto \Delta\Theta_{\text{cmd}}$, the outer loop control law

$$\delta\Theta_{\text{cmd}} \propto K_{DI} \int \Delta\dot{D_S} dt - K_{DP}\dot{D_S} \tag{22}$$

can be derived. The used TECS structure is depicted in Fig. 14. The proportional and integral gains for the specific energy rate in (19) and specific energy distribution (22) are tuned as described in [3] in order to achieve a bandwidth of 25% the inner loop bandwidth, together with satisfactory gain and phase margins as well as disturbance rejection specifications.

Fig. 15 depicts the results for the same scenario as in Fig. 10. In this scenario, the results using the TECS flight path-tracker described above are compared to the observer-based mixed sensitivity flight path-tracker designed within this work. Both approaches achieve similar performances and satisfy the tracking requirements. A satisfactory suppression of cross-coupling between FPA and airspeed is achieved.

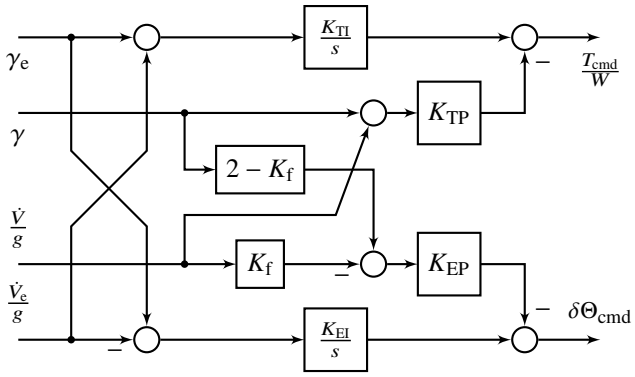

Fig. 14 TECS controller architecture.

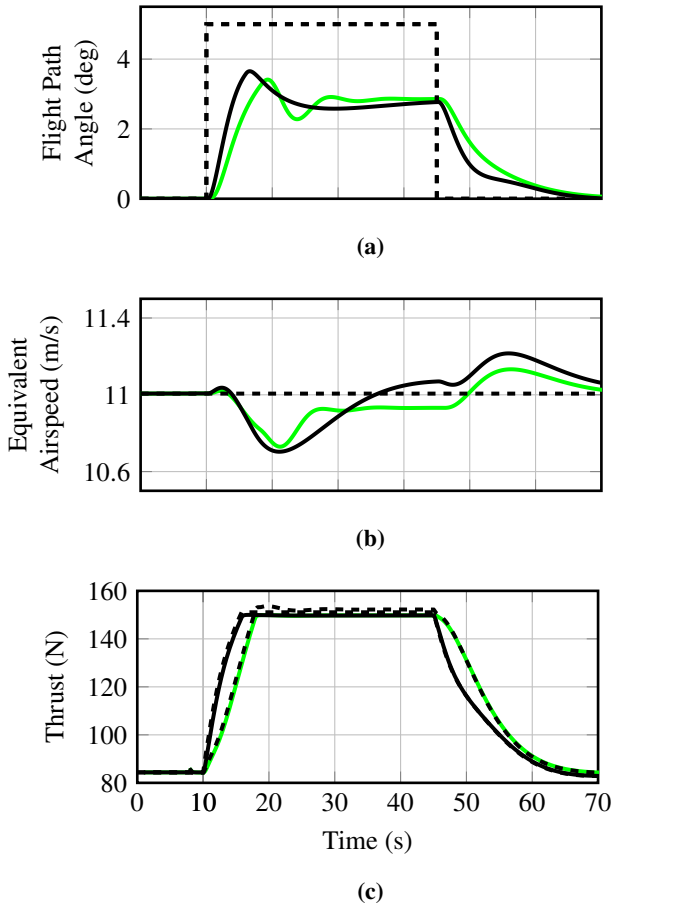

Fig. 15 Non-linear closed loop simulation of the observer-based flight path-tracker with anti-windup compensation (——) in comparison to TECS (——) for saturated thrust.

Similar to the flight path-tracker, a MC simulation is carried out for the TECS controller. The simulation setup equals the one presented in Sec. V.B and the varied parameters and their standard deviations can be found in Tab. 1. The results in Fig. 16 show that the TECS is able to prevent stall sufficiently similar to the robust observer-based controller. For the maximum measured airspeed, the MC results of the TECS controller show that in some of the disturbed simulations the

maximum allowed airspeed V_{NE} is exceeded in more than 1e-3 of the simulations. This is significantly worse than the results of the observer-based controller. Note, that the risk levels mentioned above are introduced here to give an idea of the magnitude and relations. They are not meant to be used for a certification process, but as a quantity to compare the two different controllers. Explanations for the degraded performance of the TECS controller in terms of over speed can be found within the characteristics of the HALE aircraft. On the one hand, the aircraft is highly affected by turbulence / updrafts due to its low mass, inertia and airspeed. For simulation cases in which the aircraft experiences an updraft a large positive FPA can occur quickly even though thrust is lowered to idle by the controller. On the other hand, the robust flight path-tracker was explicitly designed for keeping the airspeed error low even in presence of large FPA errors by choosing the weighting functions. The authors suggest that a similar measure, i.e. introducing a higher weighted speed priority within the TECS controller, is assumed to result in an increased performance of the TECS controller in the maximum airspeed case as well.

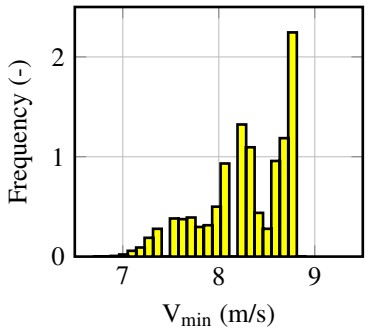

(a) PDF of the minimum equivalent airspeed.

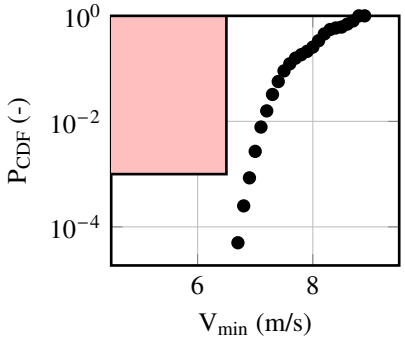

(b) CDF of the minimum equivalent airspeed.

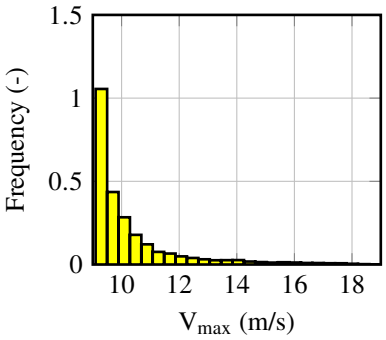

(c) PDF of the maximum equivalent airspeed.

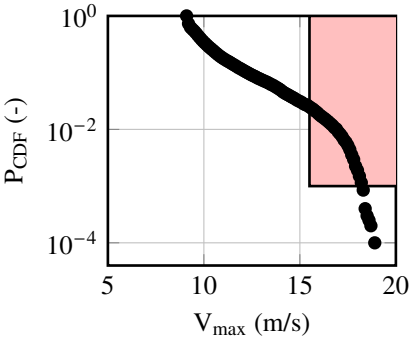

(d) CDF of the minimum equivalent airspeed.

Fig. 16 Monte-Carlo simulation results for the TECS controller.

VII. Conclusion

In this article the design and verification of a flight path-tracker for the application on a HALE aircraft is presented. The H_∞-based control design deviates from a classical H_∞ design approach so that the state feedback observer and the state feedback controller are provided explicitly. This poses the advantage in the controller implementation such that its

integrator can be isolated and anti-windup augmentation can be considered easily. The application to the HALE aircraft and the gathered results of the non-linear simulation highlight the importance of integrator windup protection for the H_∞-based control system. The results prove that the observer-based mixed sensitivity approach is capable of achieving similar results as the well-known TECS architecture in a nominal high fidelity simulation. Due to the application of standard MIMO control design methods the resulting observer-based flight path-tracker has been proven to be more robust in presence of external disturbances and model uncertainties. Finally, for the developed observer-based controller only one operating point was necessary in order to achieve sufficient performance and robustness for the full envelope.

Acknowledgements

The presented work is related to the German Aerospace Center's High Altitude Platform (HAP) project and uses design data generated therein. Currently there are 17 DLR Institutes involved in the project. The authors would like to thank especially their colleagues from the DLR Institutes of Aerodynamics and Flow Technology, Composite Structures and Adaptive Systems, Aeroelasticity and Flight Systems.

References

[1] Theis, J., Sedlmair, N., Thielecke, F., and Pfifer, H., "Observer-based LPV Control with Anti-Windup Compensation: A Flight Control Example," *IFAC-PapersOnLine*, Vol. 53, No. 2, 2020, pp. 7325–7330. https://doi.org/10.1016/j.ifacol.2020.12.988.

[2] Weiser, C., Ossmann, D., and Pfifer, H., "Robust Path-following Control with Anti-Windup for HALE Aircraft," *30th Mediterranean Conference on Control and Automation*, 2022. https://doi.org/10.1109/MED54222.2022.9837232.

[3] Weiser, C., and Ossmann, D., "Baseline Flight Control System for High Altitude Long Endurance Aircraft," *AIAA SCITECH 2022 Forum*, American Institute of Aeronautics and Astronautics, 2022. https://doi.org/10.2514/6.2022-1390.

[4] DLR, "DLR develops an unmanned stratospheric aircraft," , 2021. URL https://www.dlr.de/content/en/articles/news/2021/02/20210421_dlr-develops-an-unmanned-stratospheric-aircraft.html.

[5] Hasan, Y. J., Roeser, M. S., Hepperle, M., Niemann, S., Voß, A., Handojo, V., and Weiser, C., "Flight Mechanical Design and Analysis of a Solar-Powered High-Altitude Platform," *69. Deutscher Luft- und Raumfahrtkongress*, 2020.

[6] Voß, A., Handojo, V., Weiser, C., and Niemann, S., "Results from Loads and Aeroelastic Analyses of a High Altitude, Long Endurance, Solar Electric Aircraft," *Journal of Aeroelasticity and Structural Dynamics*, Vol. 9, No. 1, 2022, pp. 1–22. https://doi.org/10.3293/asdj.2021.58.

[7] Theis, J., and Pfifer, H., "Observer-based synthesis of linear parameter-varying mixed sensitivity controllers," *International Journal of Robust and Nonlinear Control*, Vol. 30, No. 13, 2020, pp. 5021–5039. https://doi.org/10.1002/rnc.5038.

[8] Kier, T., Looye, G., and Hofstee, J., "Development of Aircraft Flight Loads Analysis Models with Uncertainties for Pre-design Studies," *Proc. of IFASD 2005, International Forum on Aroelasticity and Structural Dynamics*, 2005.

[9] Kier, T. M., and Hofstee, J. W., "Varloads - Eine Simulationsumgebung zur Lastenberechnung eines voll Flexiblen, Freifliegenden Flugzeugs," *Deutscher Luft- und Raumfahrtkongress (DLRK)*, 2004.

[10] Voß, A., Handojo, V., Weiser, C., and Niemann, S., "Preparation of Loads and Aeroelastic Analyses of a High Altitude, Long Endurance, Solar Electric Aircraft," *Aerospace Europe Conference*, 2020.

[11] Skogestad, S., and Postlethwaite, I., *Multivariable Feedback Control*, John Wiley & Sons, 2005.

[12] Theis, J., Pfifer, H., and Seiler, P., "Robust Modal Damping Control for Active Flutter Suppression," *Journal of Guidance, Control, and Dynamics*, Vol. 43, No. 6, 2020, pp. 1056–1068. https://doi.org/10.2514/1.g004846.

[13] Glover, K., and McFarlane, D., "Robust stabilization of normalized coprime factor plant descriptions with H_∞-bounded uncertainty," *IEEE Transactions on Automatic Control*, Vol. 34, No. 8, 1989, pp. 821–830. https://doi.org/10.1109/9.29424.

[14] McFarlane, D. C., and Glover, K. (eds.), *Robust Controller Design Using Normalized Coprime Factor Plant Descriptions*, Springer-Verlag, 1990. https://doi.org/10.1007/bfb0043199.

[15] Biertümpfel, F., Theis, J., and Pfifer, H., "Observer-Based Synthesis of Finite Horizon Linear Time-Varying Controllers," *American Control Conference (ACC)*, 2022. https://doi.org/10.23919/ACC53348.2022.9867184.

[16] Åaström, K., and Hägglund, T., *PID controllers*, International Society for Measurement and Control, 1995.

[17] Blight, J. D., Dailey, R. L., and Gangsaas, D., "Practical control law design for aircraft using multivariable techniques," *International Journal of Control*, Vol. 59, No. 1, 1994, pp. 93–137. https://doi.org/10.1080/00207179408923071.

[18] Seiler, P., Packard, A., and Gahinet, P., "An Introduction to Disk Margins [Lecture Notes]," *IEEE Control Systems Magazine*, Vol. 40, No. 5, 2020, pp. 78–95. https://doi.org/10.1109/mcs.2020.3005277.

[19] anon., "MIL-HDBK-1797: Flying Qualities of Piloted Aircraft," , 2004.

[20] Hoblit, F. M., *Gust Loads on Aircraft: Concepts and Applications*, American Institute of Aeronautics and Astronautics, 1988. https://doi.org/10.2514/4.861888.

[21] Schulz, S., and Ossmann, D., "Estimation of Global Structural Aircraft Loads due to Atmospheric Disturbances for Structural Fatigure Estimation," *Proc. of IFASD 2022, International Forum on Aroelasticity and Structural Dynamics*, 2022.

[22] Lambregts, A. A., "TECS Generalized Airplane Control System Design – An Update," *Advances in Aerospace Guidance, Navigation and Control*, 2013, pp. 503–534. https://doi.org/10.1007/978-3-642-38253-6_30.

[23] Bruce, K. R., Kelly, J. R., and Person, L. H., "NASA B737 flight test results of the Total Energy Control System," Tech. rep., NASA, 1986.

[24] Kastner, N., and Looye, G., "Generic TECS Based Autopilot for an Electric High Altitude Solar Powered Aircraft," *Proceedings of the EuroGNC 2013, 2nd CEAS Specialist Conference on Guidance, Navigation & Control*, 2013, pp. 1324–1343.